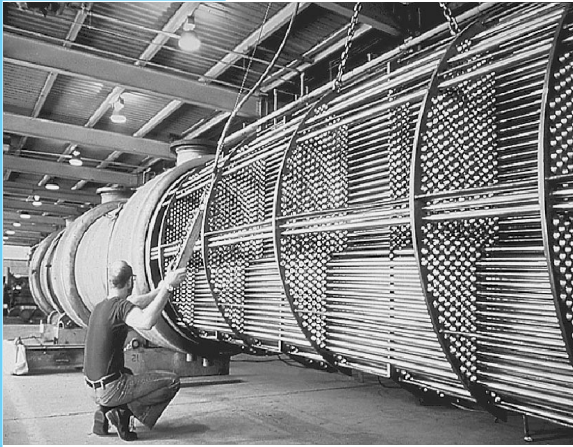


# PART FOUR

# CHAPTER 19

## Environmental Degradation



*This heat exchanger for the chemical processing industry contains over 17 kilometers of zirconium tubing. Zirconium is the material selected for many such applications due to its strong corrosion resistance in a variety of acidic and basic chemical environments. (Courtesy of Teledyne Wah Chang, Albany, Oregon.)*

y = oxide thickness

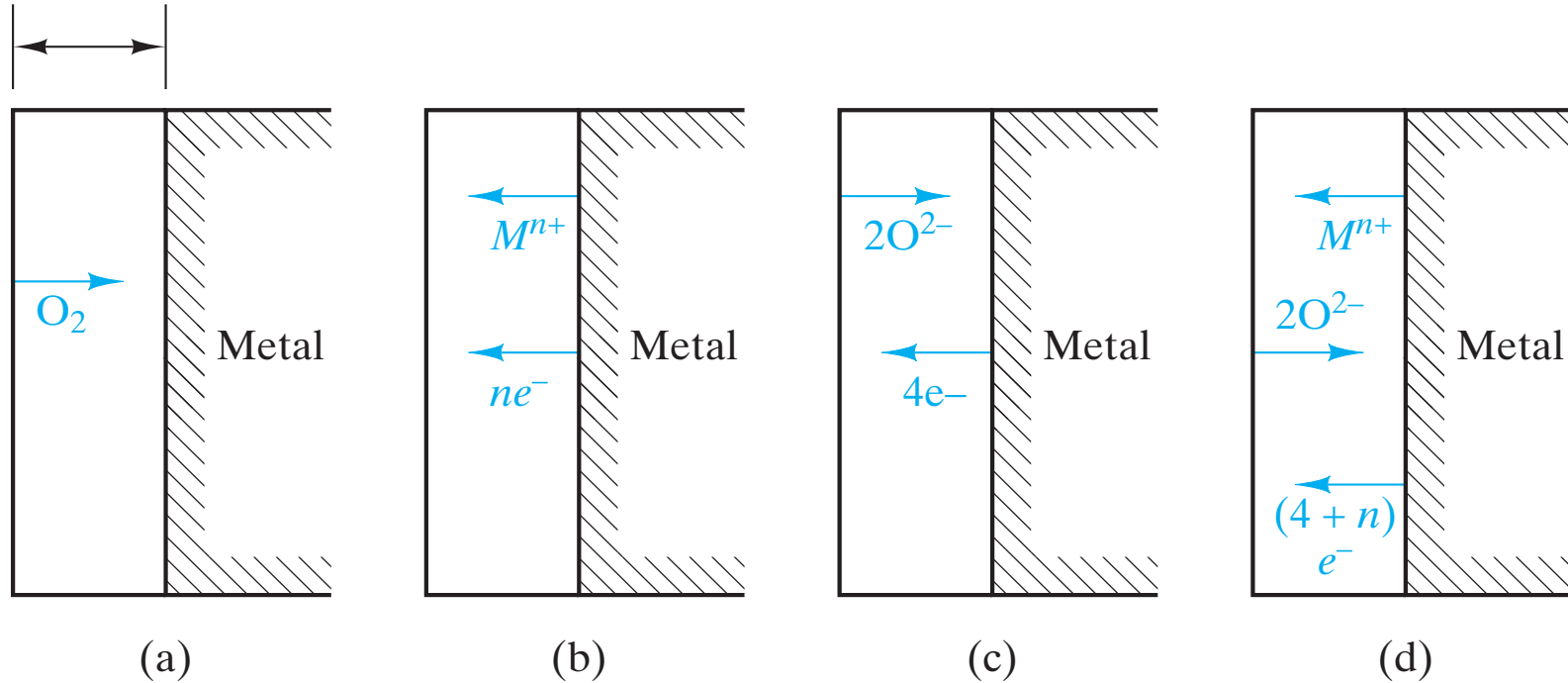


**Figure 19-1** Four possible metal oxidation mechanisms. (a) “Unprotective” film is sufficiently porous to allow continuous access of molecular  $O_2$  to the metal surface. Mechanisms (b)-(d) represent non-porous films that are “protective” against  $O_2$  permeation. In (b), cations diffuse through the film reacting with oxygen at the outer surface. In (c),  $O^{2-}$  ions diffuse to the metal surface. In (d), both cations and anions diffuse at nearly equal rates, leading to the oxidation reaction occurring within the oxide film.

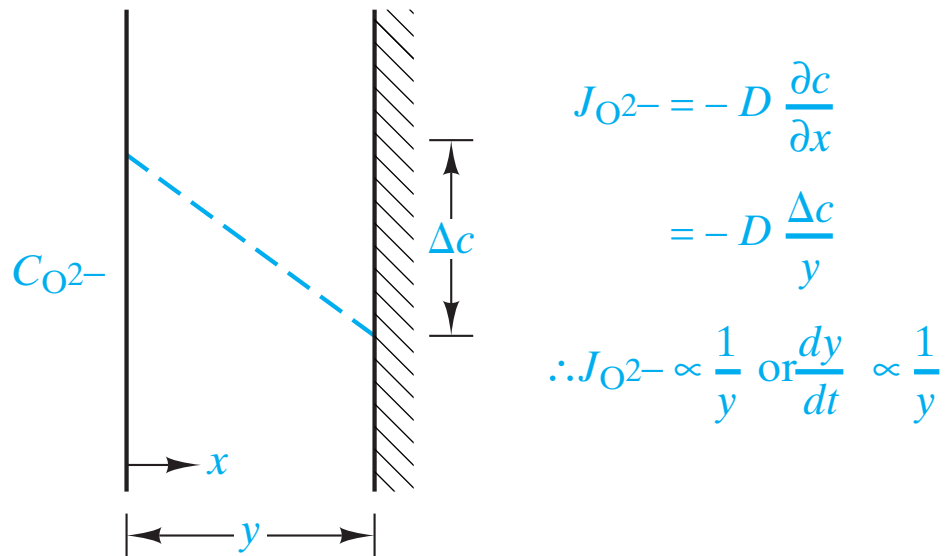


**Figure 19-2** A linear drop in oxygen concentration across the oxide film thickness leads to a film growth rate that is inversely proportional to film thickness.

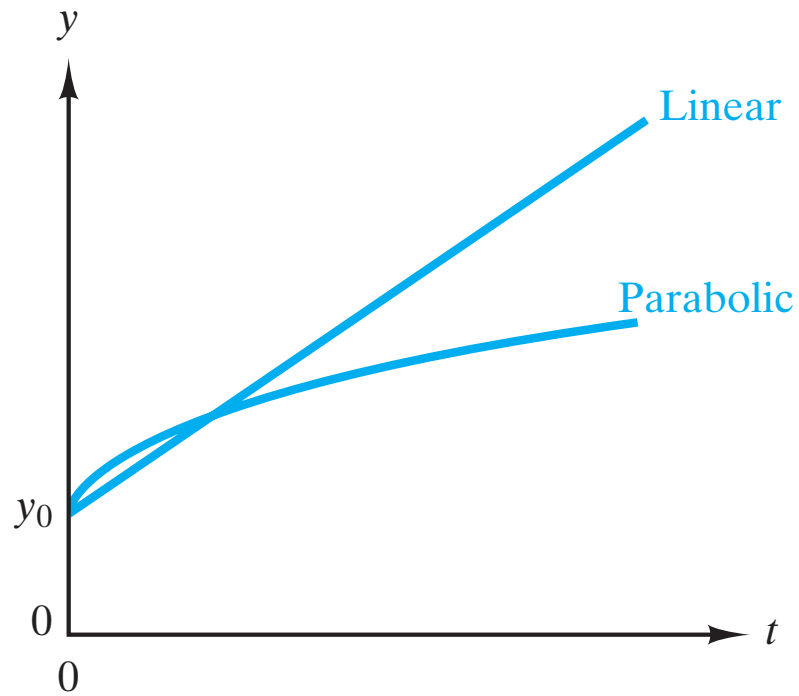


**Figure 19-3** Comparison of film growth kinetics for linear and parabolic growth laws. The diminishing growth rate with time for parabolic growth leads to protection against further oxidation.

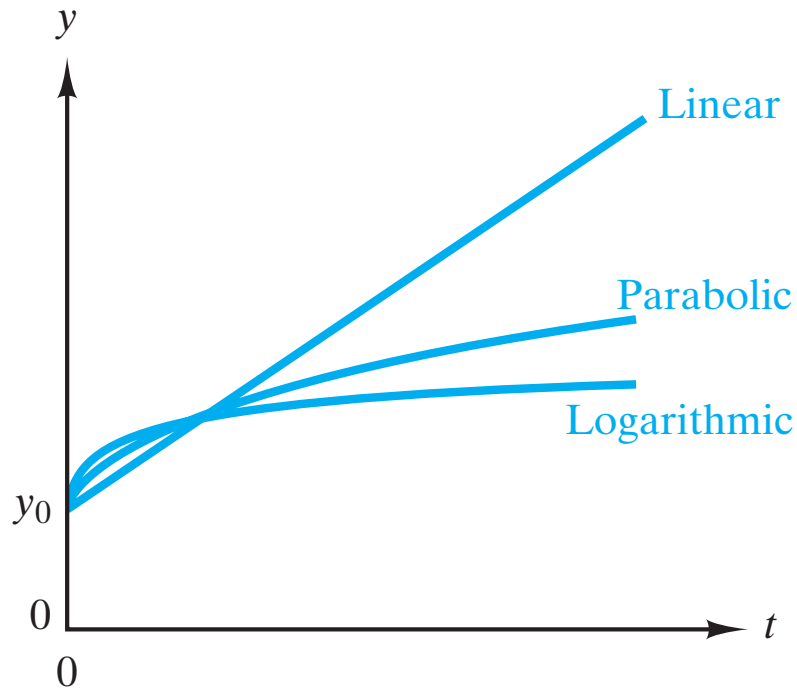


**Figure 19-4** A logarithmic growth rate law is superimposed on the linear and parabolic growth law plots of Figure 19-3. The logarithmic kinetics applies primarily to thin oxide films at low temperatures and provides little benefit for corrosion resistance.

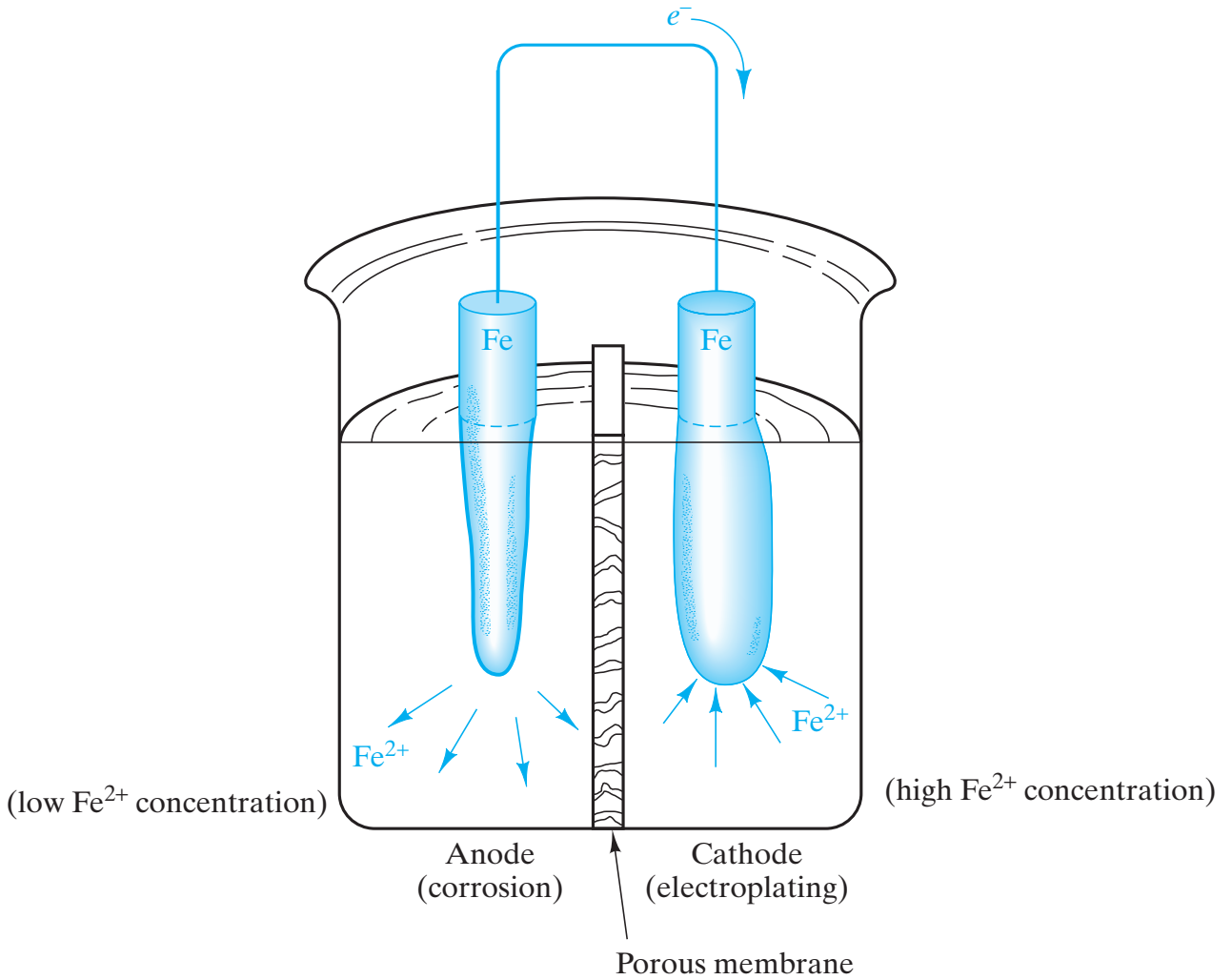


**Figure 19-5** In this electrochemical cell, corrosion occurs at the anode, and electroplating occurs at the cathode. The driving force for the two “half-cell” reactions is a difference in ionic concentration.

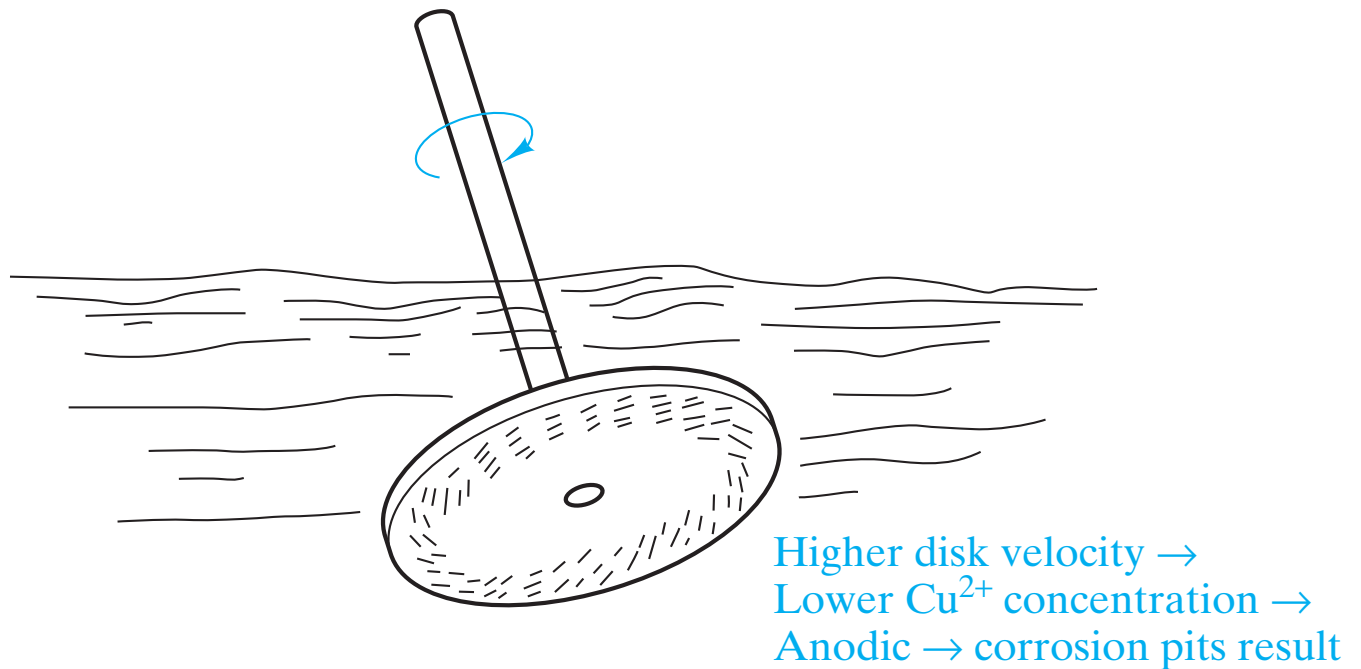


**Figure 19-6** A rotating brass disk in an aqueous solution containing  $\text{Cu}^{2+}$  ions produces a gradient in ionic concentration near its surface. The  $\text{Cu}^{2+}$  concentration is lower next to the more rapidly moving surface near the disk edge. As a result, that area is anodic and corrodes. This problem is analogous to the ionic concentration cell in Figure 19-5.

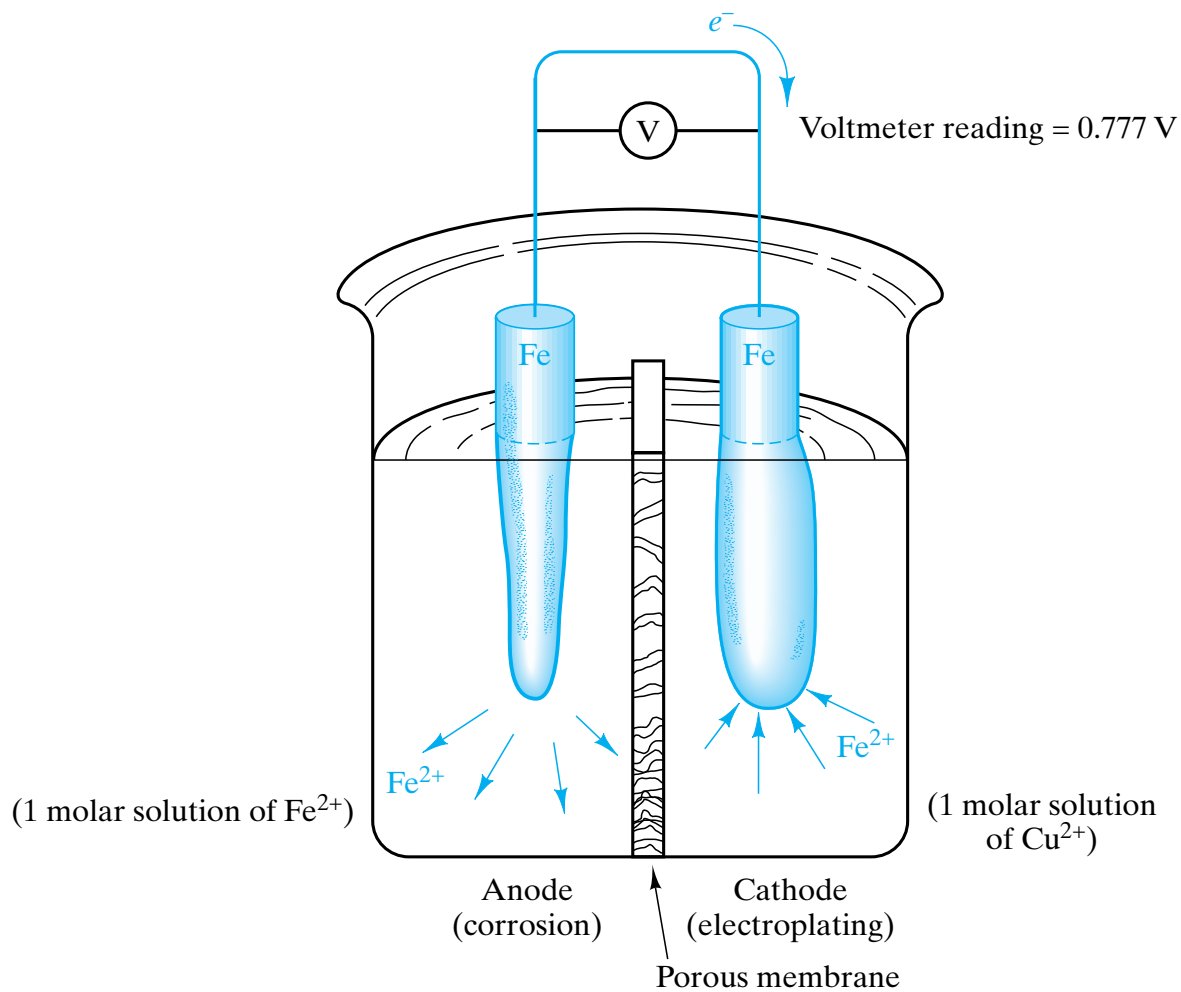


**Figure 19-7** A galvanic cell is produced by two dissimilar metals. The more “anodic” metal corrodes.

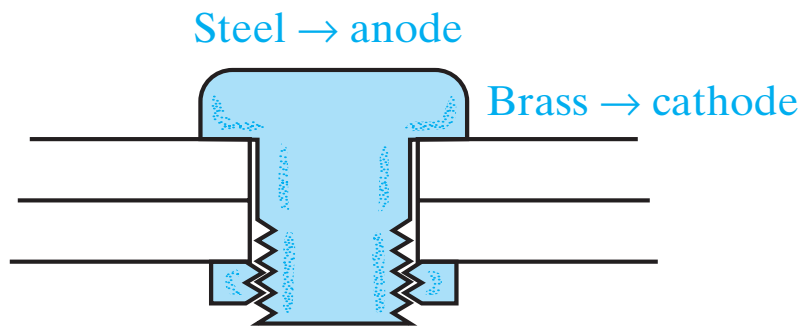


**Figure 19-8** *A steel bolt in a brass plate creates a galvanic cell analogous to the model system in Figure 19-7.*

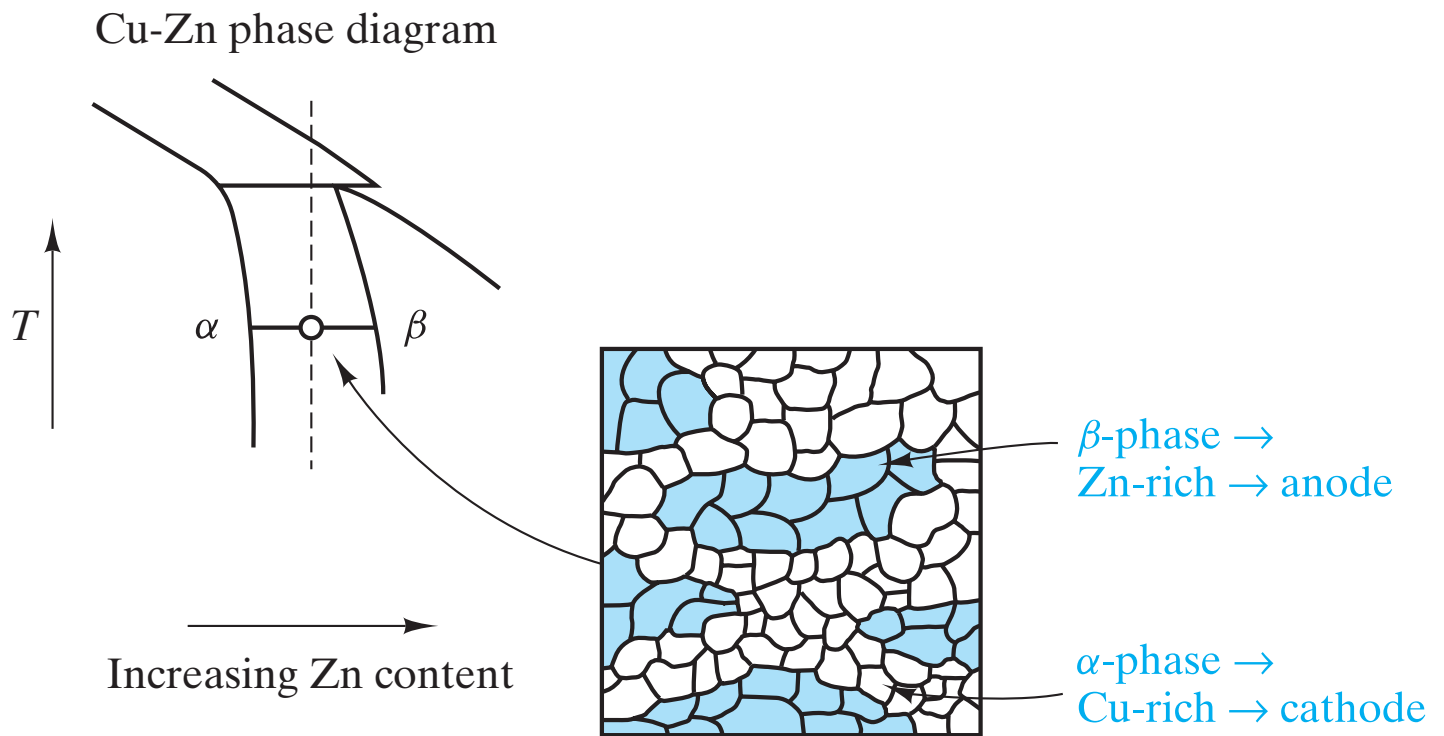


**Figure 19-9** A galvanic cell can be produced on the microscopic scale. Here  $\beta$ -brass (bcc structure) is zinc-rich and anodic relative to  $\alpha$ -brass (fcc structure), which is copper-rich.

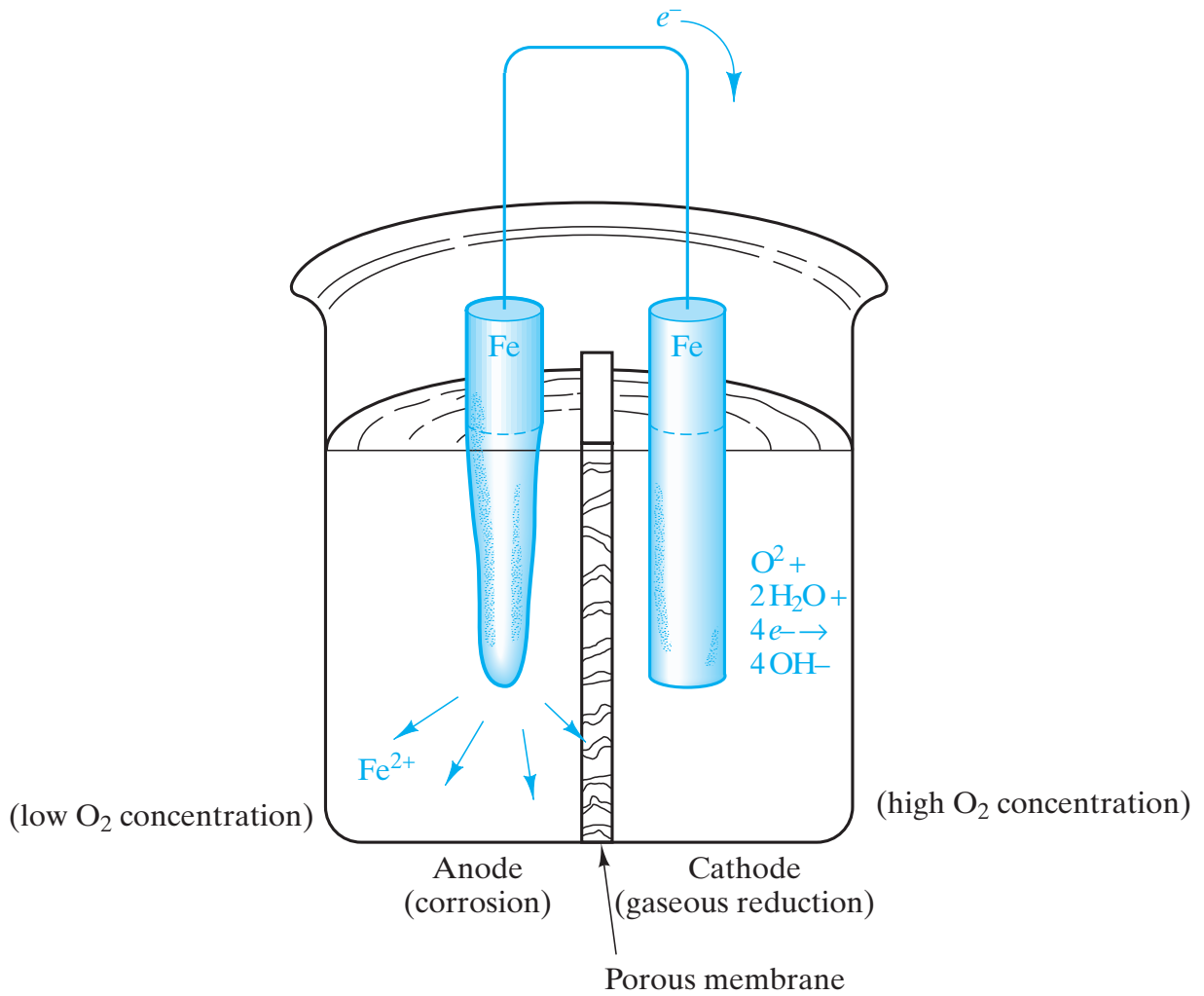


**Figure 19-10** In an oxygen concentration cell, the driving force for reaction is the difference in oxygen concentration. Corrosion occurs at the oxygen-deficient anode. The cathodic reaction is gaseous reduction.

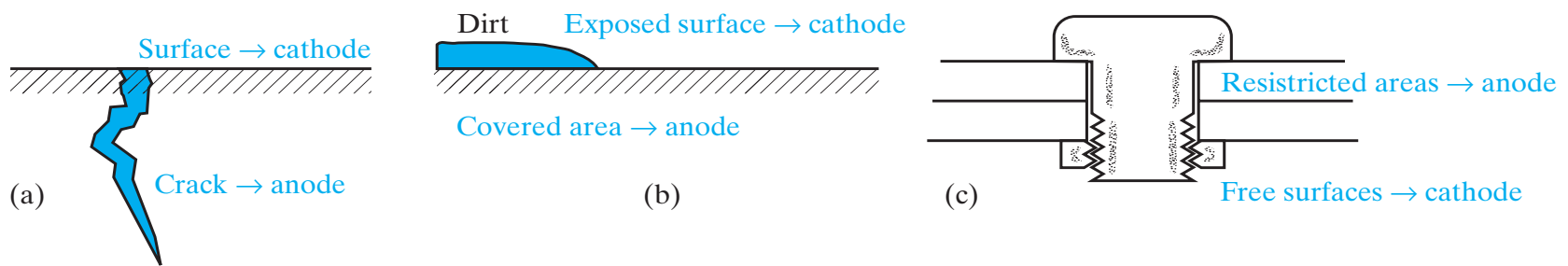


**Figure 19-11** Various practical examples of corrosion due to oxygen concentration cells. In each case, metal corrodes next to oxygen-deficient regions of an aqueous environment.

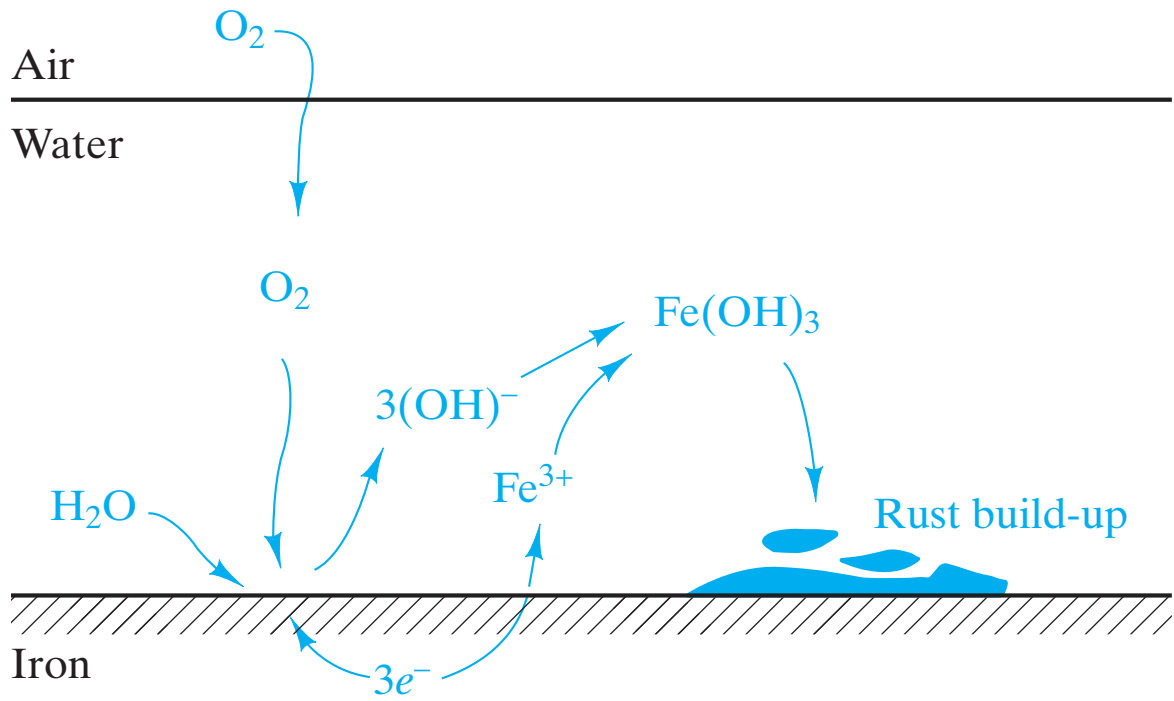


**Figure 19-12** *The rusting of ferrous alloys is another corrosion reaction associated with gaseous reduction.*

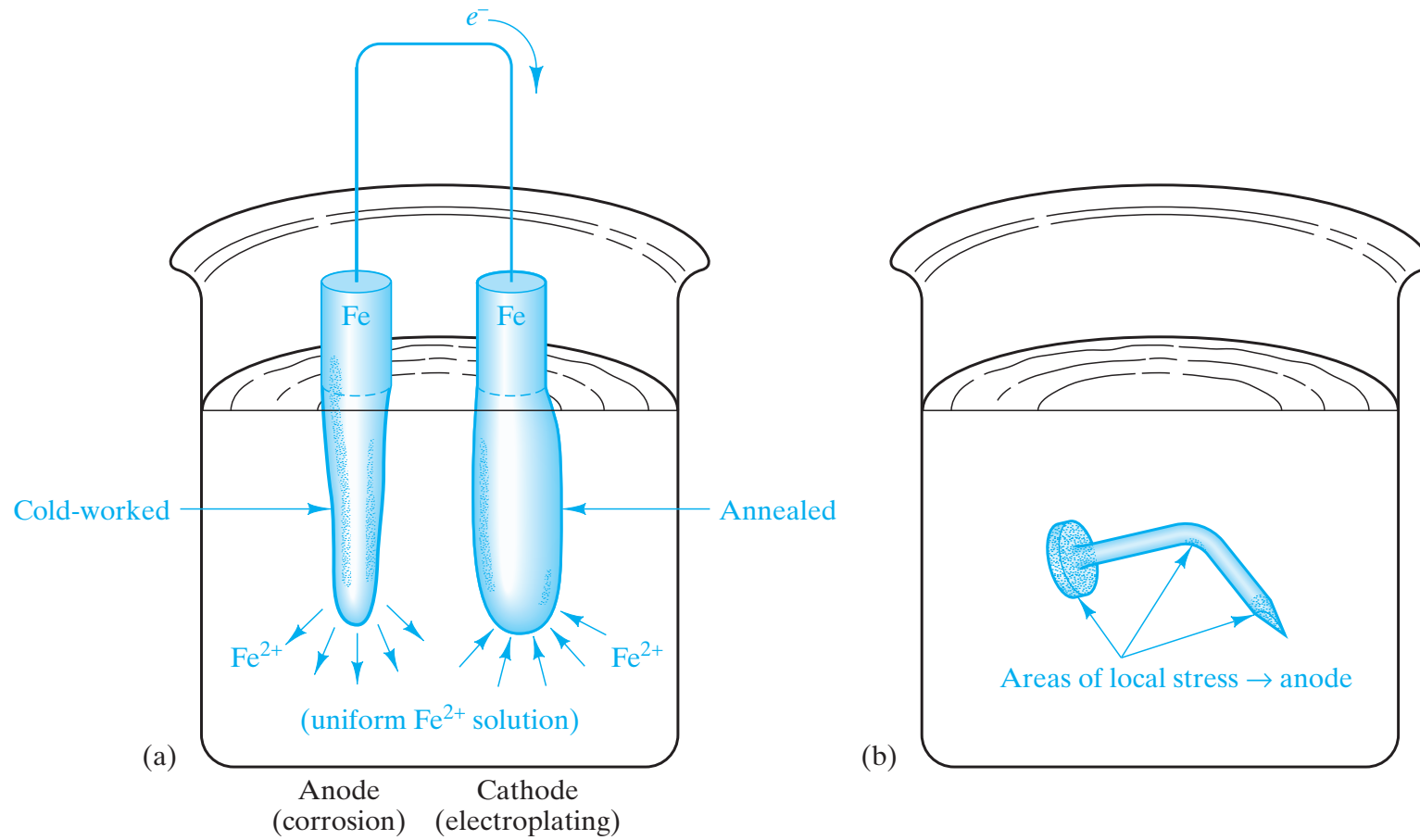


**Figure 19-13** (a) Model electrochemical stress cell. The more highly stressed electrode is anodic and corrodes. (b) Common example of a stress cell. In an aqueous environment, the regions of a nail that were stressed during fabrication or use corrode locally.

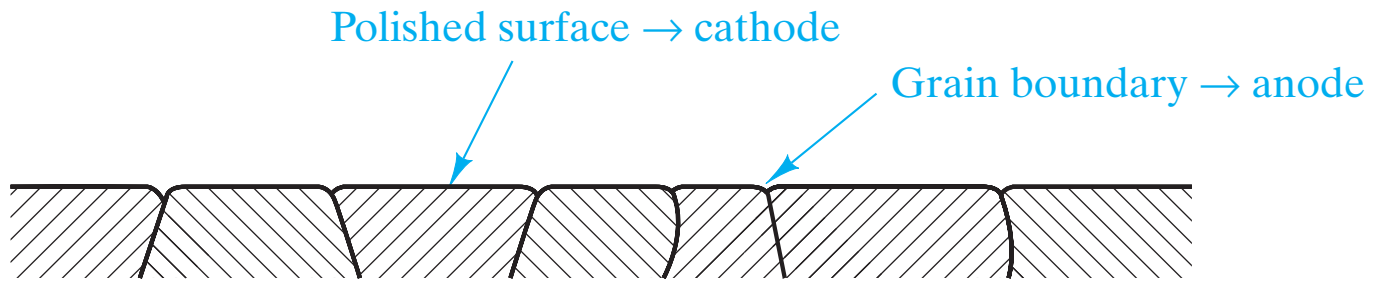
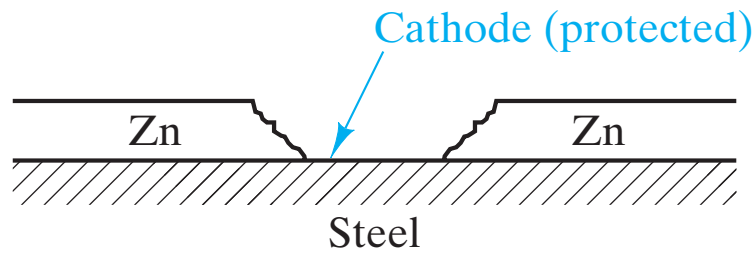
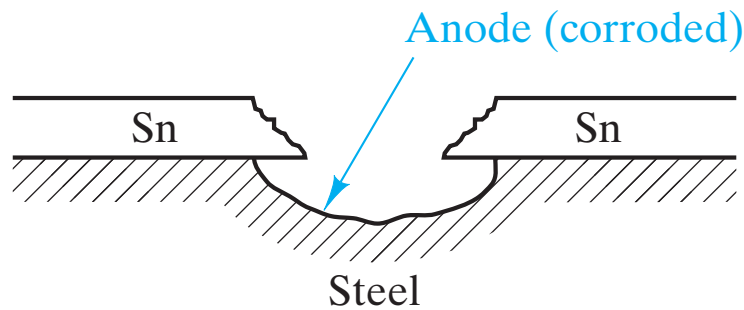


**Figure 19-14** *On the microscopic scale, grain boundaries are regions of local stress and are susceptible to accelerated attack.*



(a)



(b)

**Figure 19-15** (a) Galvanized steel consists of a zinc coating on a steel substrate. Since zinc is anodic to iron, a break in the coating does not lead to corrosion of the substrate. (b) In contrast, a more noble coating such as “tin plate” is protective only as long as the coating is free of breaks. At a break, the anodic substrate is preferentially attacked.

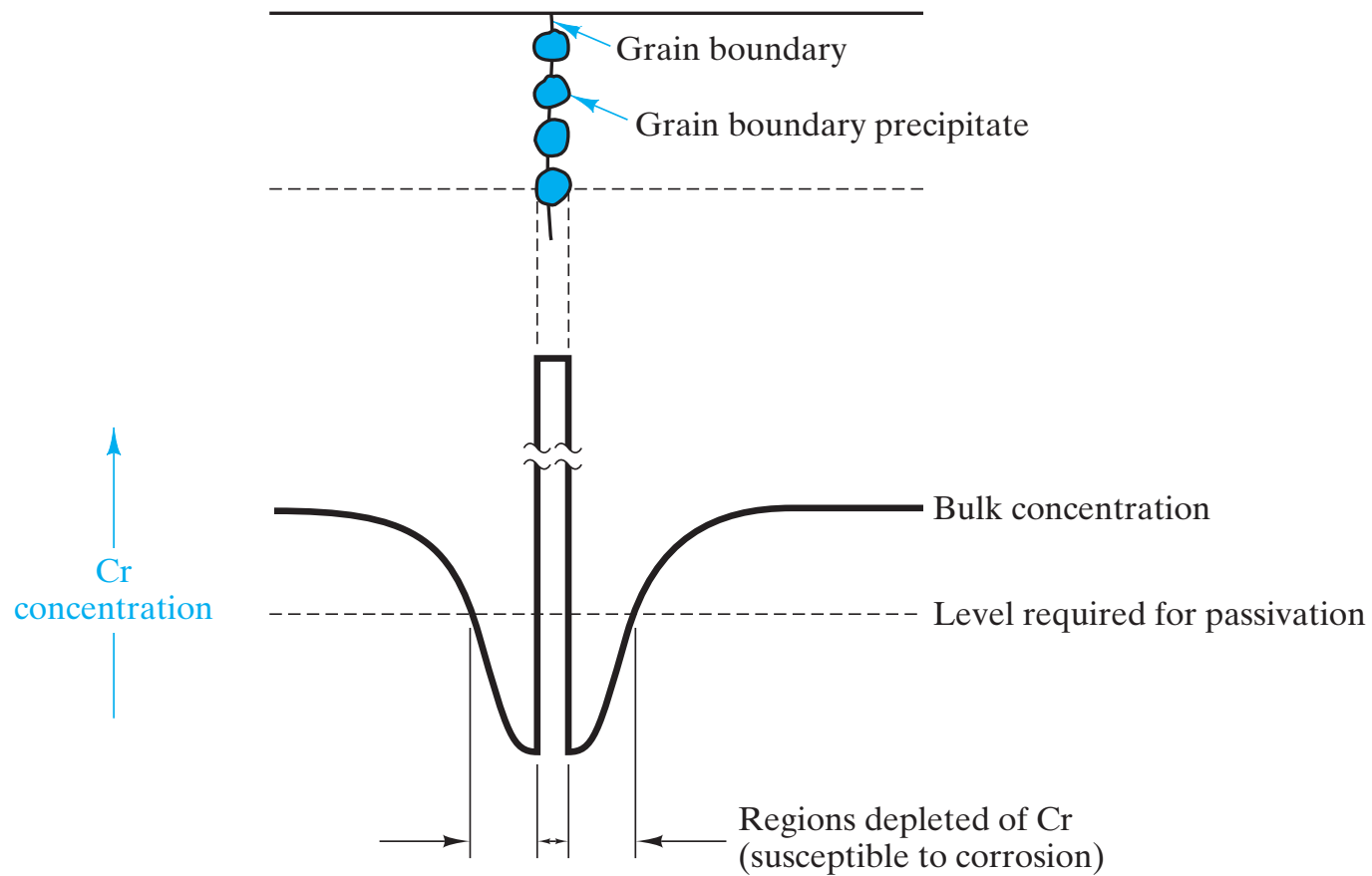


**Figure 19-16** Heating a stainless steel can cause precipitation of chromium carbide particles, leaving adjacent regions of the microstructure depleted in chromium and thereby susceptible to corrosion. This effect is the basis of the common warning to avoid welding of stainless steel components.

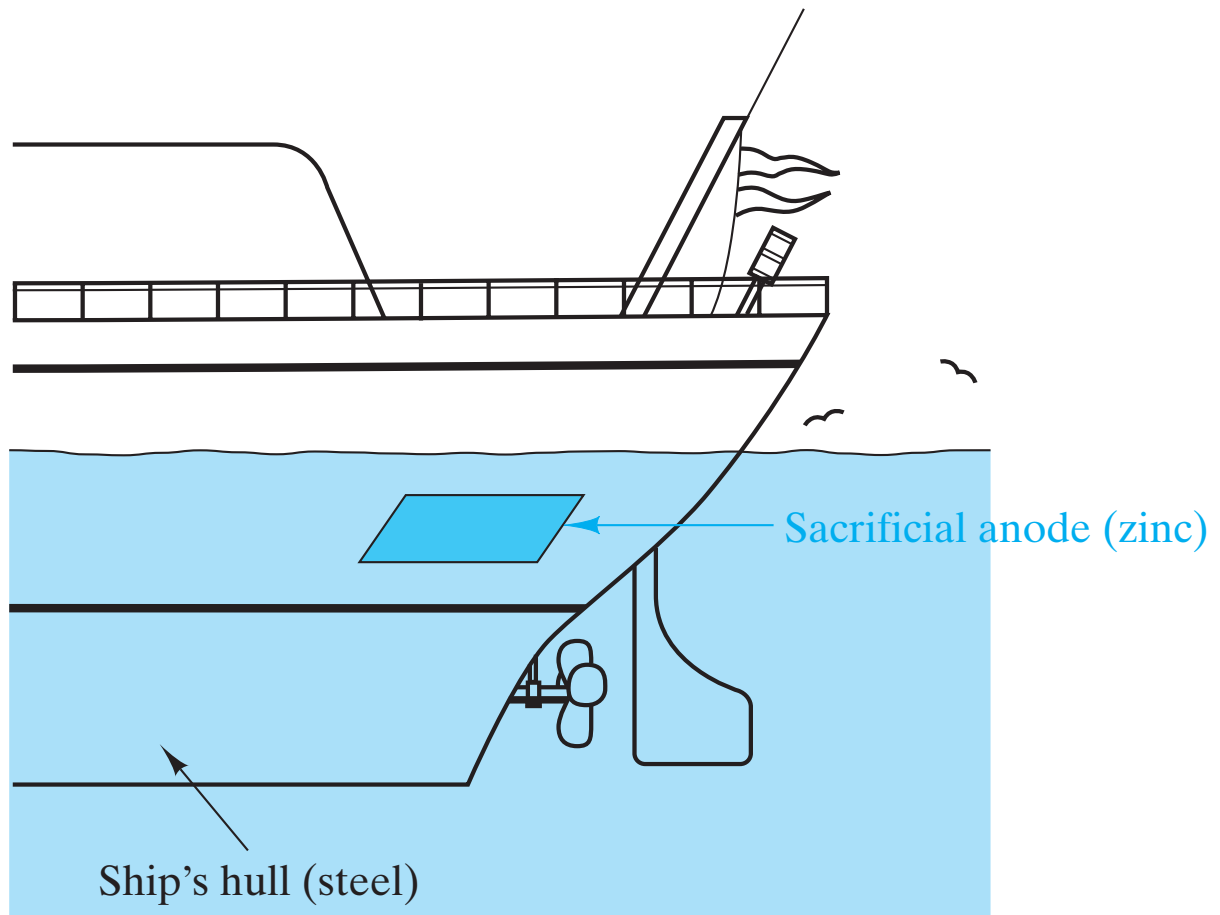
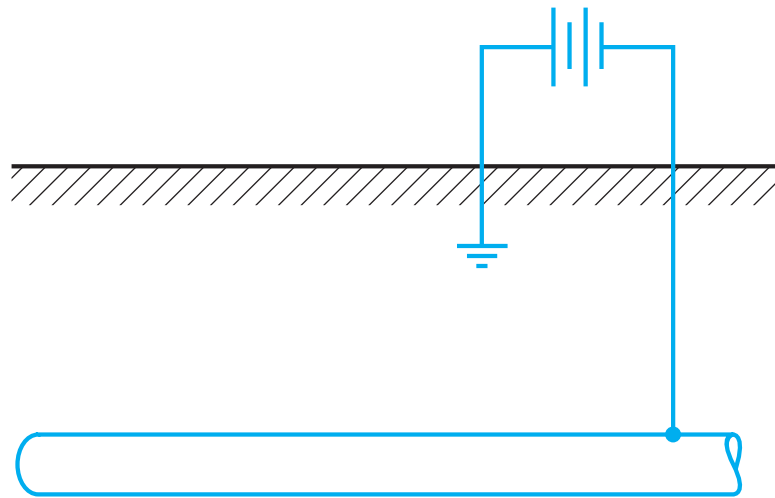


**Figure 19-17** *A sacrificial anode is a simple form of galvanic protection. The galvanized steel in Figure 19-15a is a special form of this protection.*



Underground pipe

**Figure 19-18** *An impressed voltage is a form of galvanic protection that counters the corroding potential.*

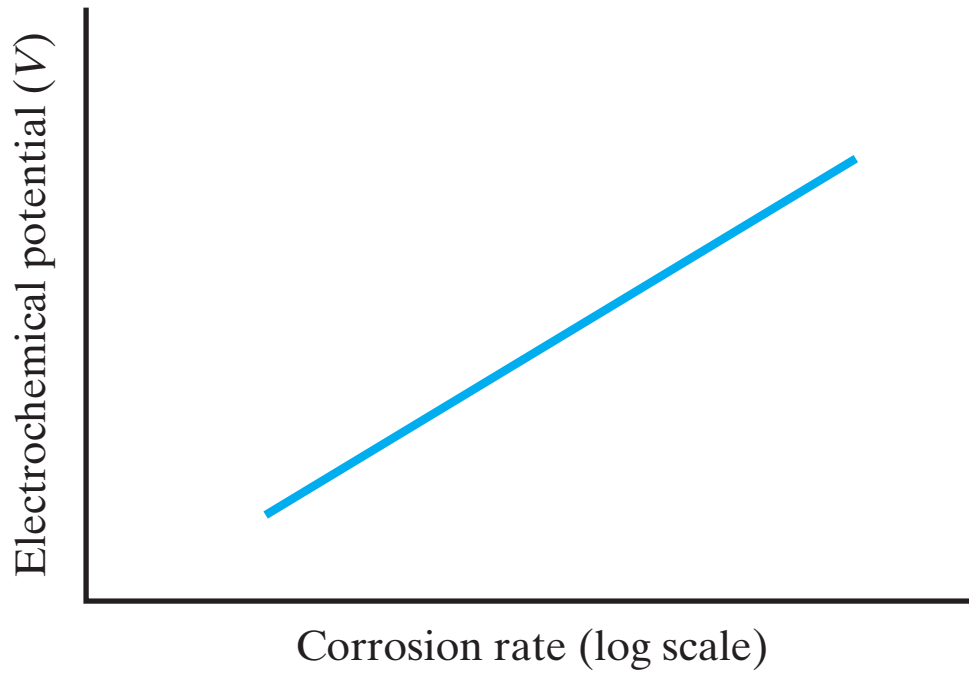


**Figure 19-19** *Schematic illustration of the linear, semilogarithmic plot of electrochemical potential versus corrosion rate for an anodic half-cell.*

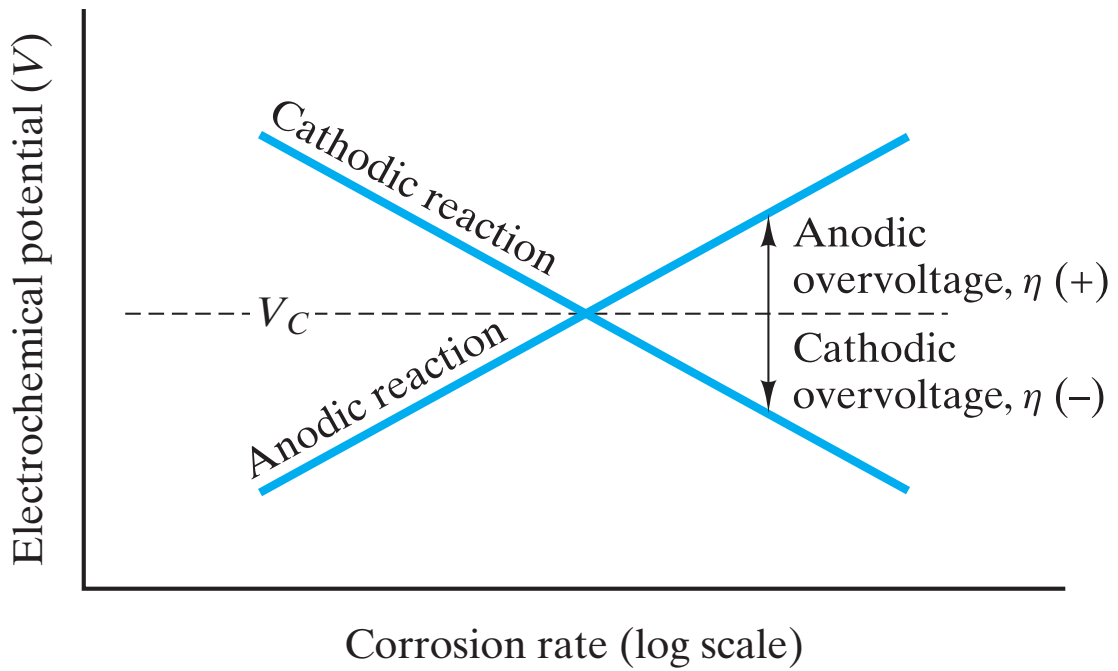


**Figure 19-20** Schematic illustration of the establishment of a corrosion potential,  $V_c$ , at the intersection of anodic and cathodic reaction plots. Anodic polarization corresponds to a positive overvoltage,  $\eta$ .

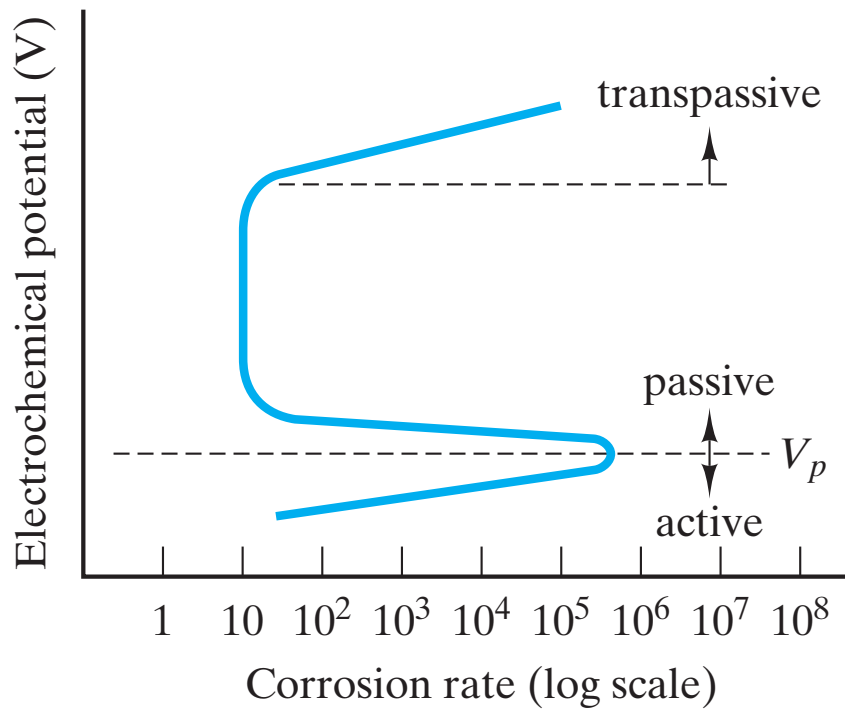


**Figure 19-21** Schematic illustration of passivity. The corrosion rate for a given metal drops sharply above an oxidizing potential of  $V_p$ .

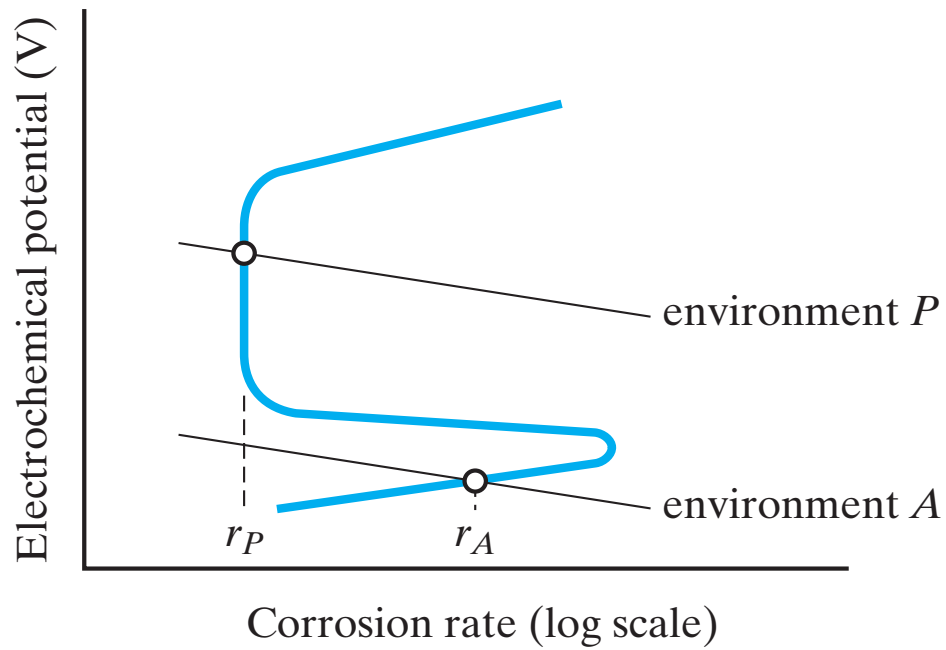


**Figure 19-22** *The position of a cathodic half-cell plot can affect the nature of metallic corrosion. Environment A intersects the anodic polarization curve in the active region, and environment P intersects in the passive region.*

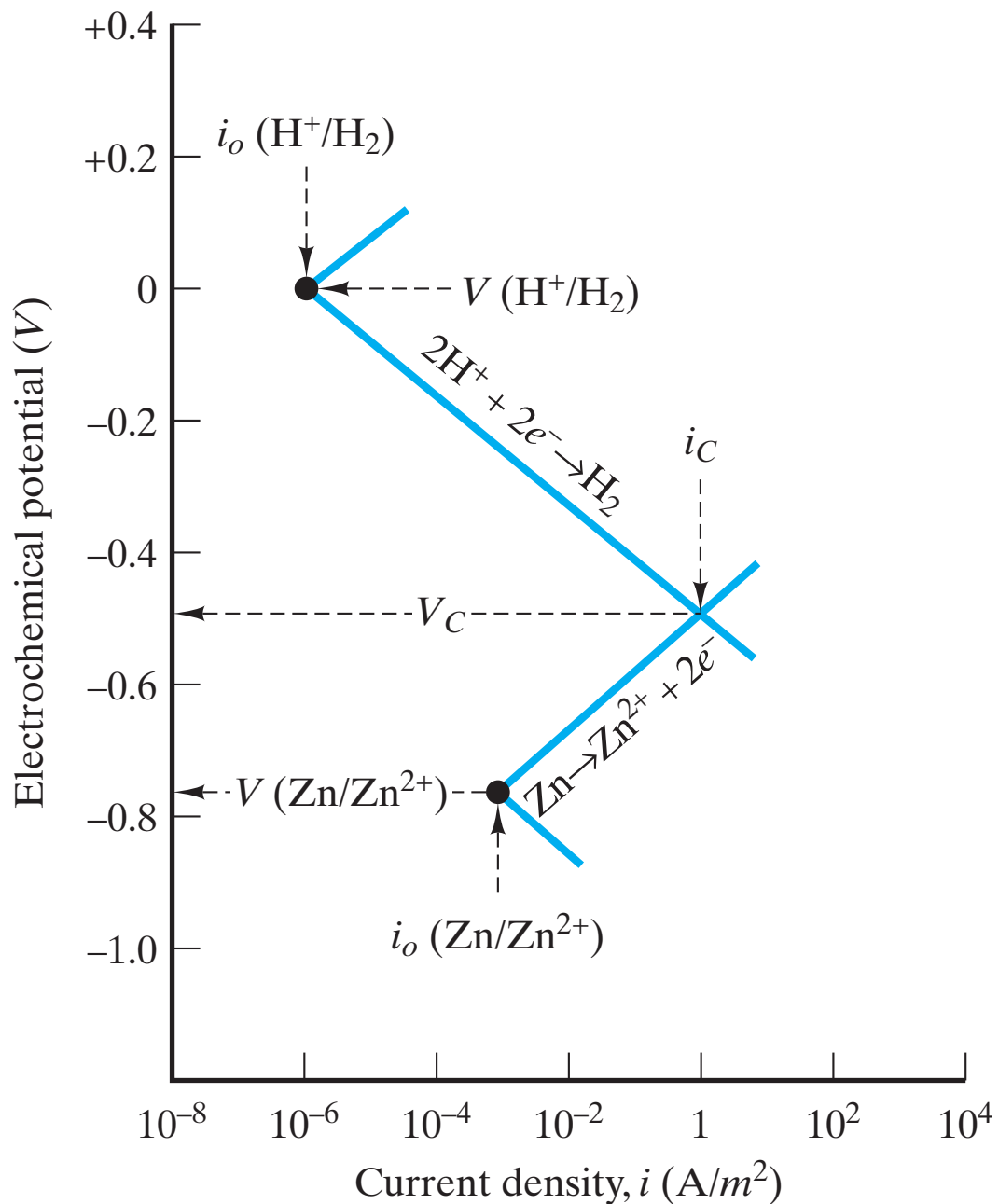


**Figure 19-23** The anodic and cathodic half-cell reactions for zinc in an acid solution show, by their intersection, the corrosion potential,  $V_c$ , and corrosion current density,  $i_c$ . (After M. G. Fontana, *Corrosion Engineering*, 3rd ed., McGraw-Hill, New York, 1986.)

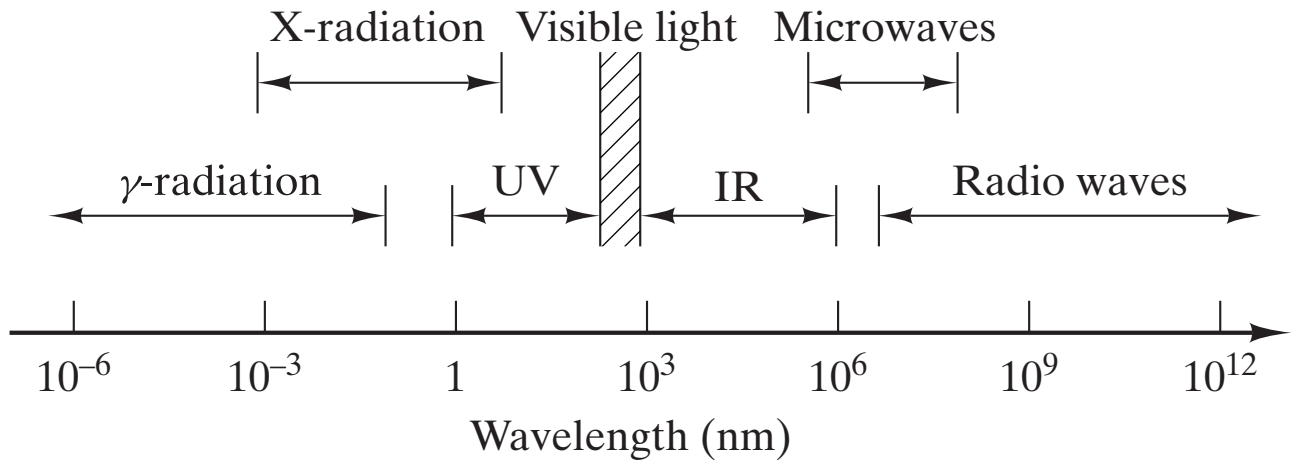


**Figure 19-24** *Electromagnetic radiation spectrum. (This chart was introduced in Figure 3–34 in which x-radiation was first described as a medium for identifying crystalline structures and later in Figure 16–1 as an introduction to the optical behavior of materials.)*

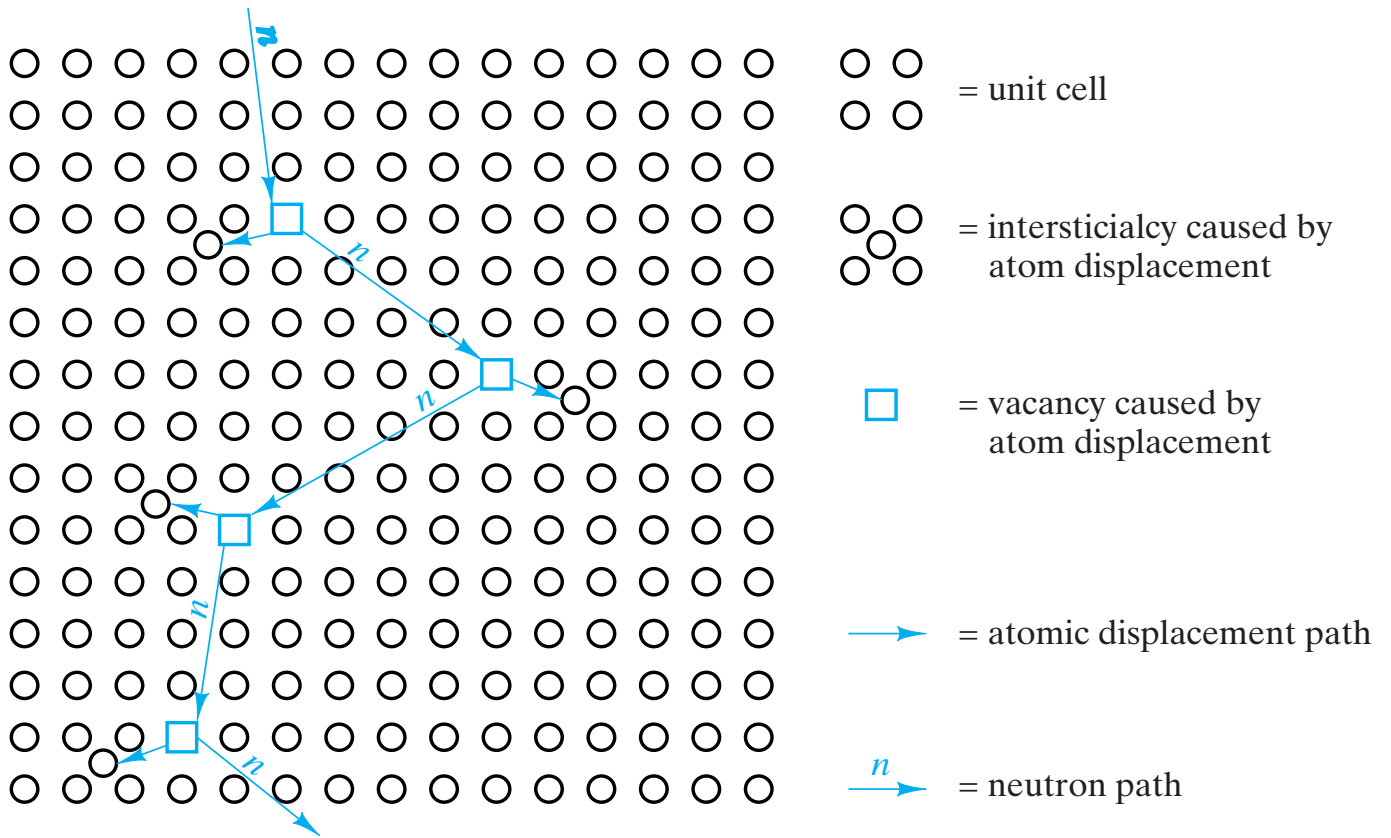


**Figure 19-25** Schematic of the sequence of atomic displacements in a metallic crystal structure caused by a single, high-energy neutron. (An electron micrograph of a neutron-damaged microstructure of a zirconium alloy is shown in Figure 4-35a.)

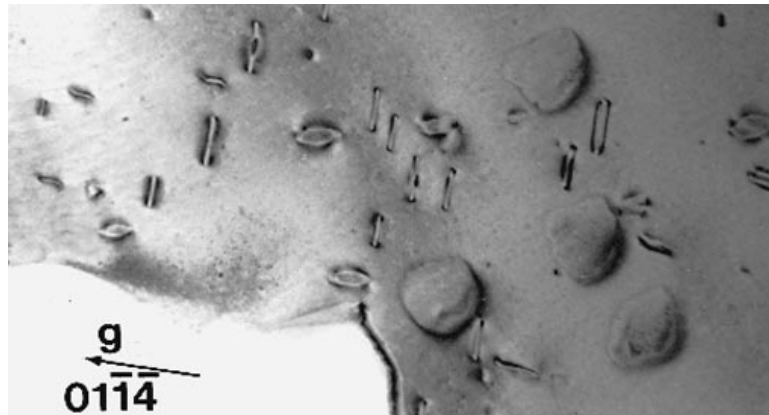


**Figure 19-26** *Electron micrograph of dislocation loops produced in  $\text{Al}_2\text{O}_3$  as a result of electron beam irradiation. (Courtesy of D. G. Howitt)*

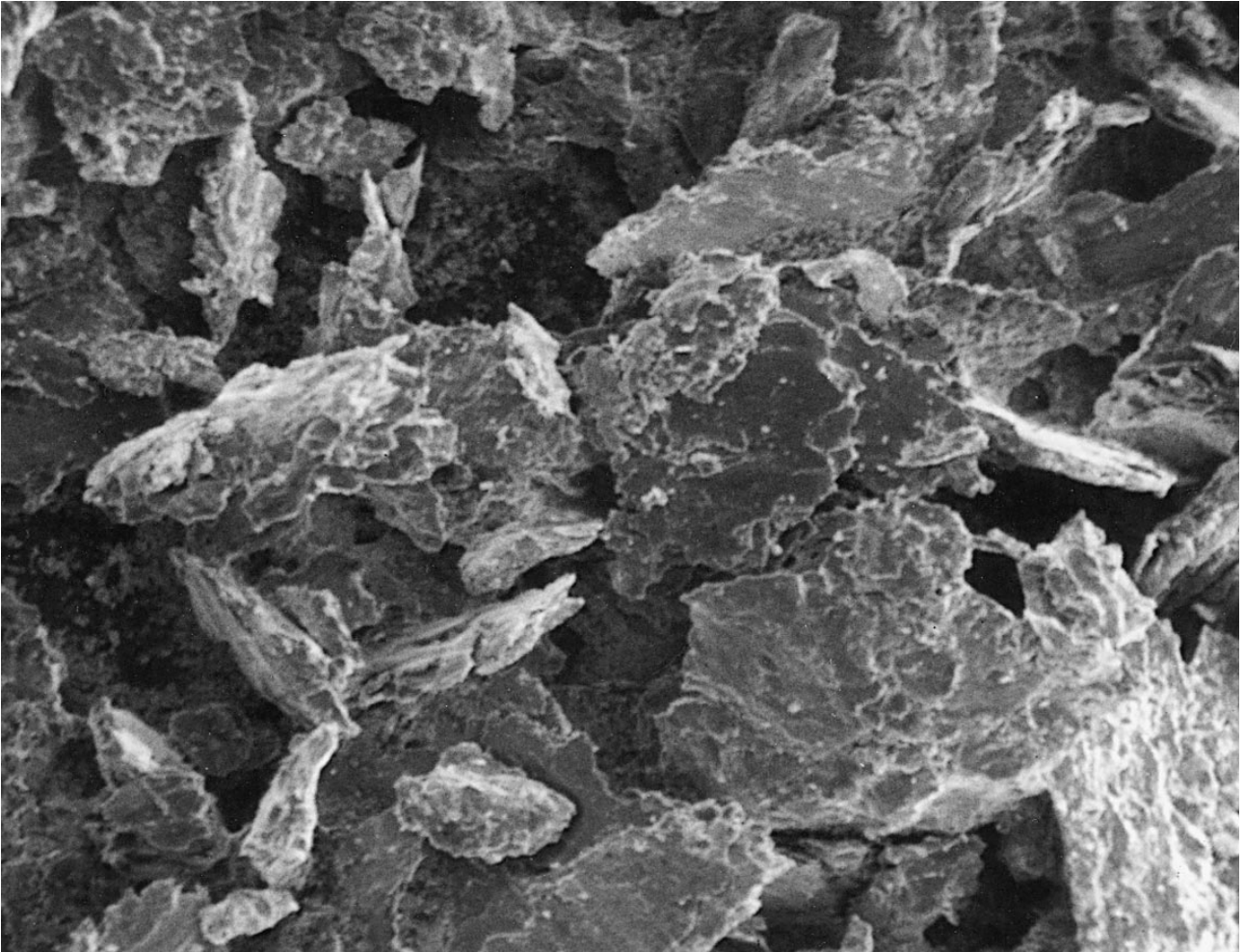


**Figure 19-27** *The sliding of a copper disk against a 1020 steel pin produces irregular wear particles. (Courtesy of I. F. Stowers)*

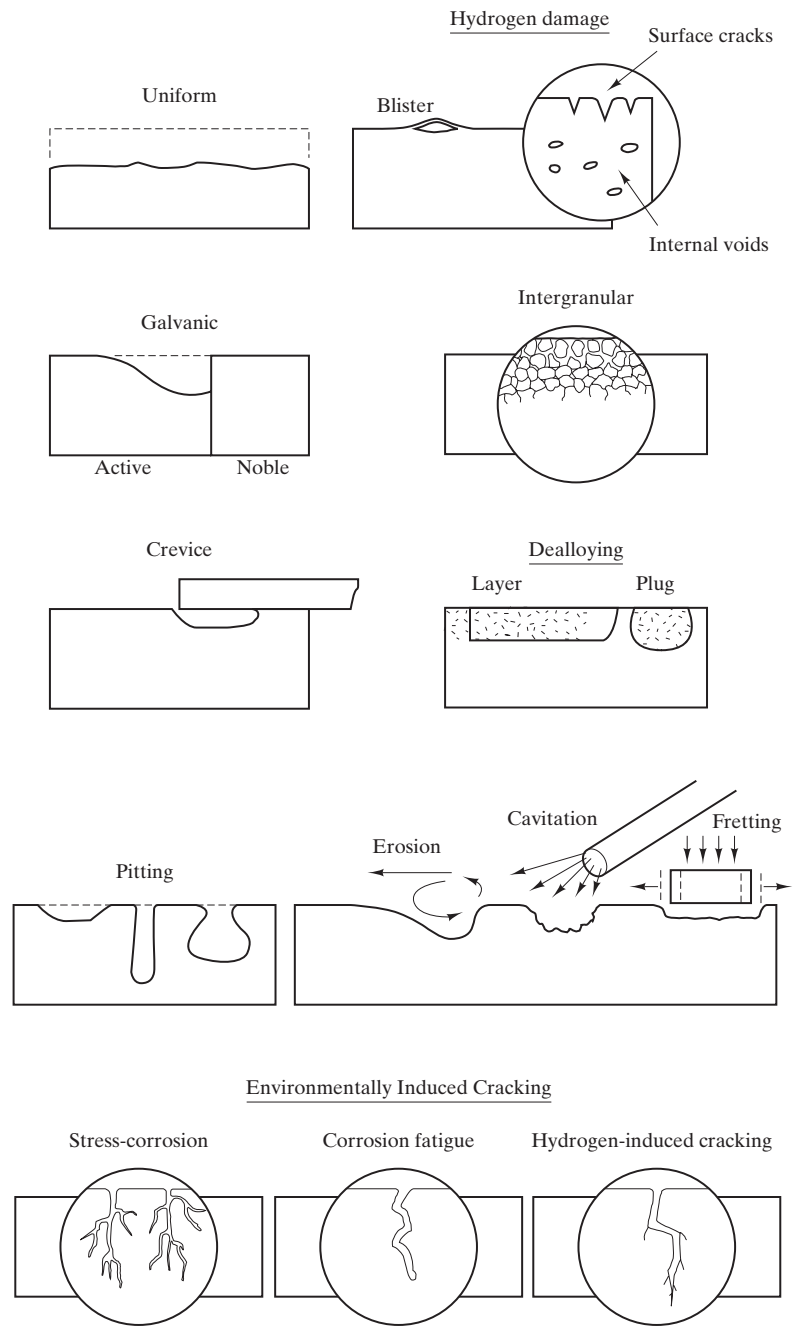


**Figure 19-28** Schematic summary of the various forms of environmental degradation for metals. (From D. A. Jones, *Principles and Prevention of Corrosion*, Macmillan Publishing Company, New York, 1992.)

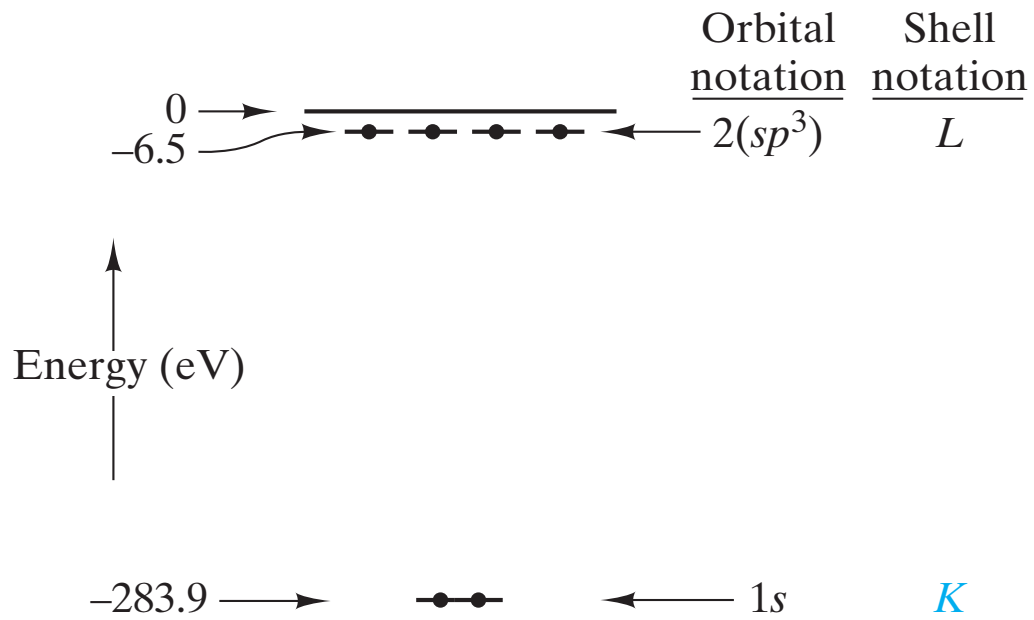


**Figure 19-29** The energy level diagram for a carbon atom (introduced in Figure 2–3) is labeled with a  $K$  for the lowest energy (innermost) electron shell and an  $L$  for the next lowest energy shell.

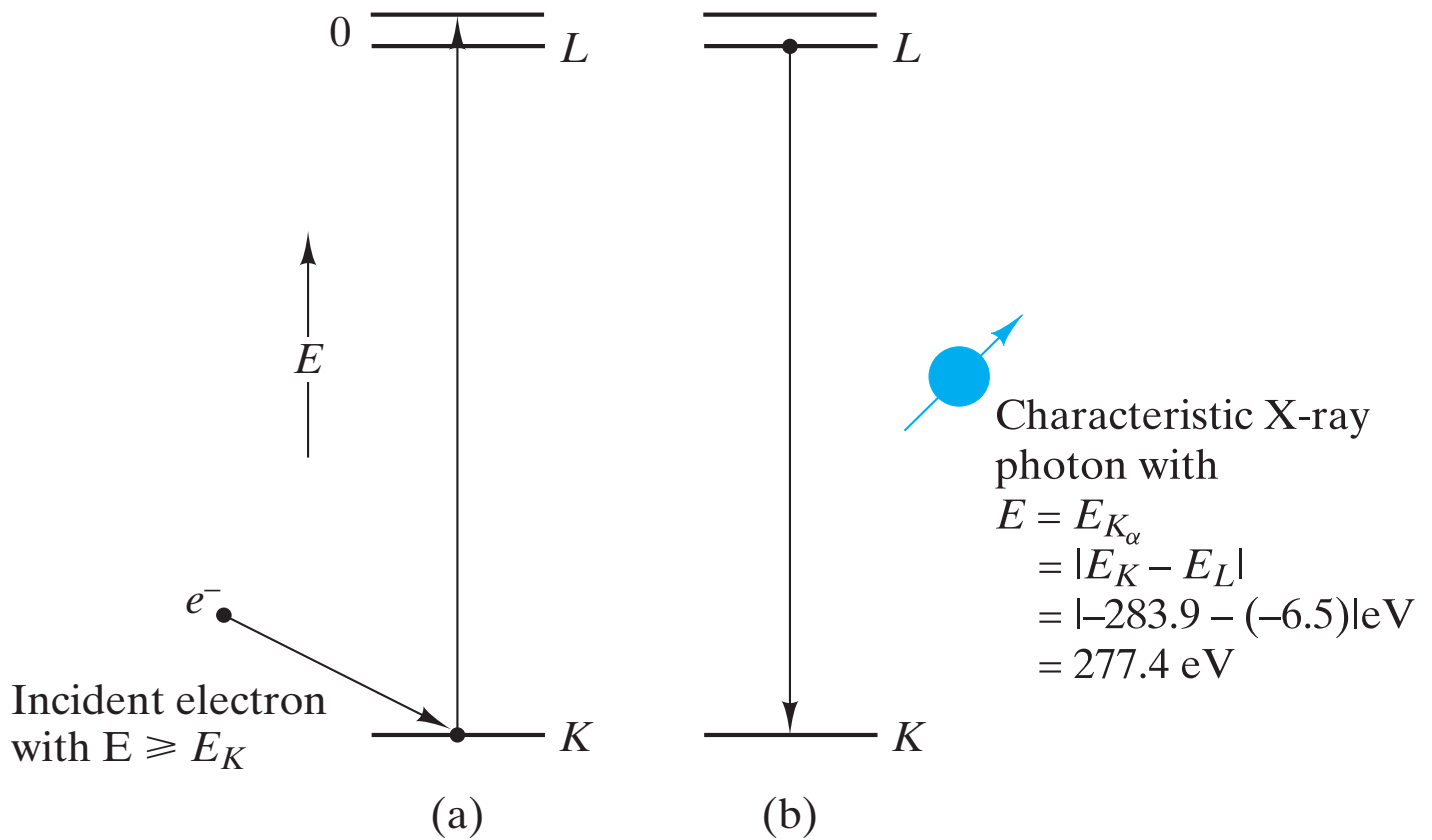


**Figure 19-30** The mechanism for producing a characteristic x-ray photon for chemical analysis of an atom of the element carbon can be represented in two steps. (a) An electron with energy greater than or equal to the binding energy of a K shell electron (283.9 eV) can eject that electron from the atom. (b) The resulting unstable state is eliminated by an L to K electron transition. The reduction in electron energy produces a  $K_\alpha$  photon with a specific energy characteristic of the carbon atom.

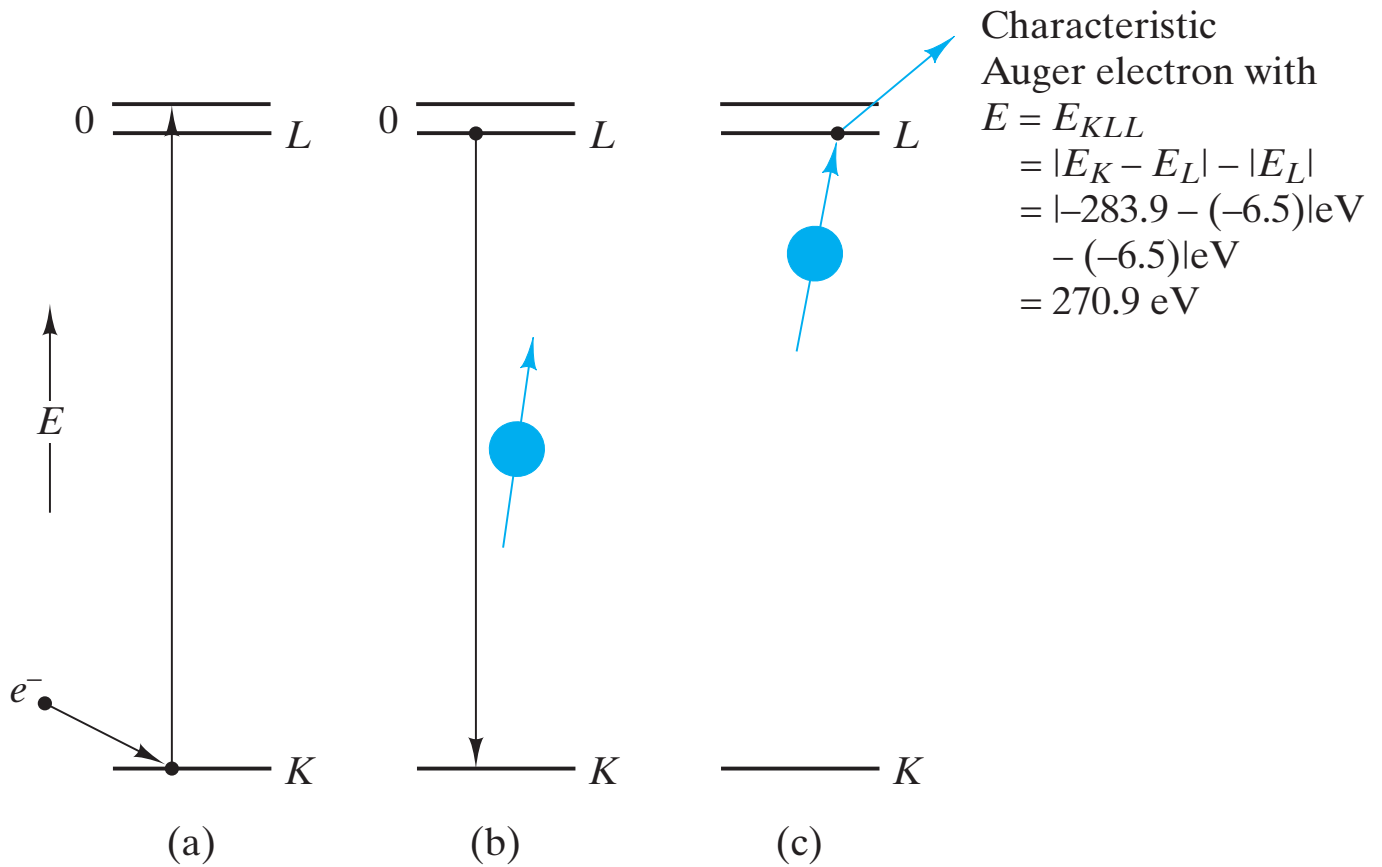


**Figure 19-31** The mechanism for producing a characteristic electron for chemical analysis of a carbon atom in the first few atomic layers of a sample surface can be represented in three steps. Steps (a) and (b) are essentially identical to Figure 19-30. In step (c), the characteristic  $K_{\alpha}$  photon ejects an L shell electron. The resulting kinetic energy of this Auger electron has a specific value characteristic of the carbon atom.



**Figure 19-32** *A commercial microprobe for doing scanning Auger electron spectroscopy. (Courtesy of Perkin-Elmer, Physical Electronics Division)*

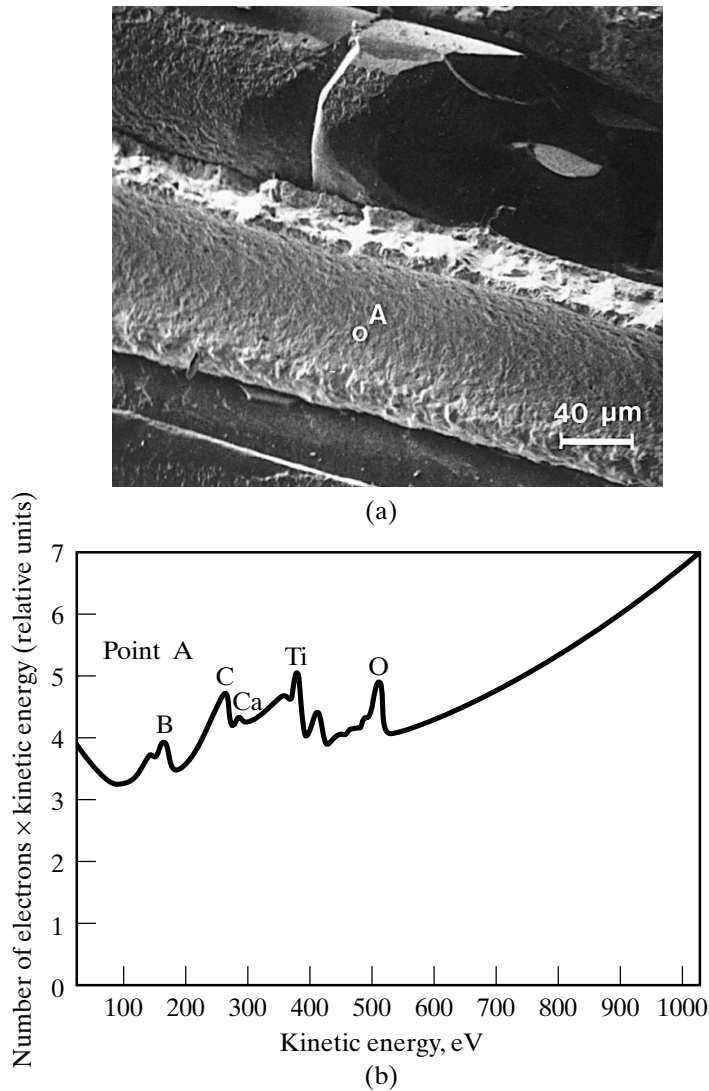
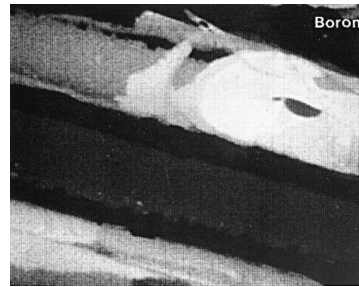
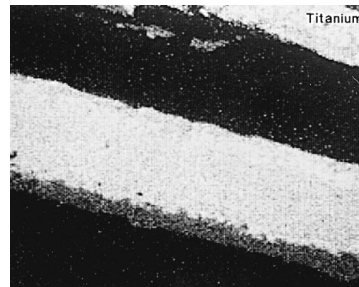


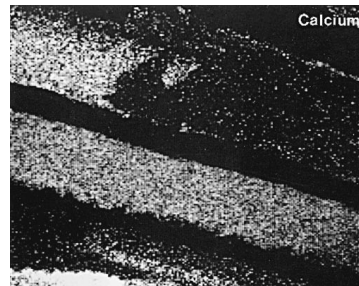
**Figure 19-33** (a) Scanning electron image of the fracture surface of a composite of boron carbide fibers in a titanium matrix. (b) Auger electron spectrum measured at point A in the image of part (a). Note the magnitude of the kinetic energy of the carbon Auger electron as calculated in Figure 19-31. Note also the presence of Ca and O impurities at the fracture interface. (Courtesy of Perkin-Elmer, Physical Electronics Division)



(a)



(b)



(c)

**Figure 19-34** (a) Boron, (b) titanium, and (c) calcium maps of the fracture surface shown in Figure 14-33a at the same magnification. These Auger electron images can be powerful indicators of impurity concentrations [such as calcium in (c)] confined within a few atomic layers at the interface between the composite matrix and the reinforcing phase. Such interfacial segregation can play a major role in material properties, such as fracture strength. (Courtesy of Perkin-Elmer, Physical Electronics Division)

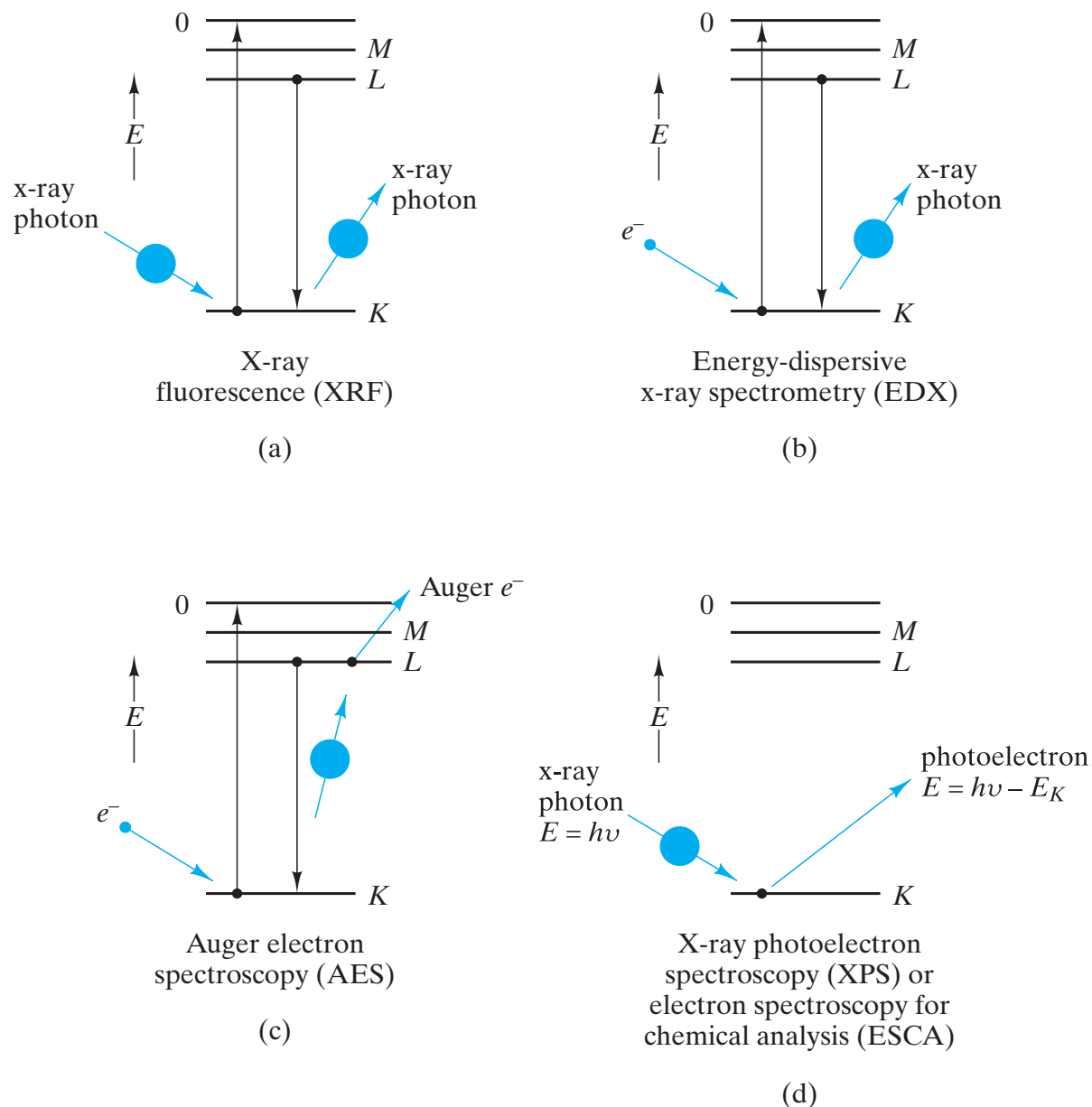


**Figure 19-35** Schematic illustration summarizing the four, related techniques for surface chemical analysis given in Table 19.7. Note that (a) x-ray fluorescence and (b) energy-dispersive x-ray spectrometry essentially involve bulk chemical analysis, whereas (c) Auger electron spectroscopy and (d) x-ray photoelectron spectroscopy (or electron spectroscopy for chemical analysis) represent true surface analysis, providing the analysis of the outermost atomic layer(s).